



Article

<https://doi.org/10.1038/s41567-024-02460-w>

Polarity-driven three-dimensional spontaneous rotation of a cell doublet

Received: 21 December 2022

Accepted: 29 February 2024

Published online: 13 May 2024

Linjie Lu ^{1,2,3,4,11}, Tristan Guyomar ^{1,2,3,4,11}, Quentin Vagne ^{5,11}, Rémi Berthoz ^{1,2,3,4}, Alejandro Torres-Sánchez ⁶, Michèle Lieb ^{1,2,3,4}, Cecilie Martin-Lemaitre ^{7,8}, Kobus van Unen ⁹, Alf Honigmann ^{7,8,10}, Olivier Pertz ⁹, Daniel Riveline ^{1,2,3,4} & Guillaume Salbreux ⁵

Check for updates

Mechanical interactions between cells play a fundamental role in the self-organization of organisms. How these interactions drive coordinated cell movement in three dimensions remains unclear. Here we report that cell doublets embedded in a three-dimensional extracellular matrix undergo spontaneous rotations. We investigate the rotation mechanism and find that it is driven by a polarized distribution of myosin within cell cortices. The mismatched orientation of this polarized distribution breaks the doublet mirror symmetry. In addition, cells adhere at their interface through adherens junctions and with the extracellular matrix through focal contacts near myosin clusters. We use a physical theory describing the doublet as two interacting active surfaces to show that rotation is driven by myosin-generated gradients of active tension whose profiles are dictated by interacting cell polarity axes. We also show that three-dimensional shape symmetries are related to broken symmetries of the myosin distribution in cortices. To test for the rotation mechanism, we suppress myosin clusters using laser ablation and generate new myosin clusters by optogenetics. Our work clarifies how polarity-oriented active mechanical forces drive collective cell motion in three dimensions.

Spontaneous cell rotational motions have been reported in a variety of contexts *in vivo*. For instance, tissues undergo rotation during development in *Drosophila* in the egg chamber¹, in the ommatidia of the retina², in the genitalia³ and in zebrafish embryos, where rotation of cell pairs occurs in the zebrafish's lateral line⁴. In early *Caenorhabditis elegans* embryo development, chiral counter-rotating flows break chiral symmetry and play a role in setting the organism's left-right axis^{5,6}.

Seminal observations *in vitro* in two dimensions have shown that endothelial adhering cells migrating on a substrate and confined within a two-dimensional pattern form a stably rotating doublet⁷. The cell-cell

interface adopts a curved shape, such that the doublet acquires an overall shape reminiscent of a 'yin-yang' symbol. More recently, groups of epithelial cells were reported to undergo rotation within rings^{8,9}. In three dimensions *in vitro*, during alveogenesis of human mammary gland organoids, it has been shown that branches also undergo rotation¹⁰. In addition, Madin–Darby canine kidney (MDCK) cells can assemble into hollow cysts in three dimensions, which undergo spontaneous rotation in an assay within two layers of Matrigel¹¹. There, the two layers of Matrigel impose a polarization axis to the cyst, which allows one to probe for chiral broken symmetry, revealed in a bias in the direction of

¹Institut de Génétique et de Biologie Moléculaire et Cellulaire, Illkirch, France. ²Université de Strasbourg, Illkirch, France. ³Centre National de la Recherche Scientifique, Illkirch, France. ⁴Institut National de la Santé et de la Recherche Médicale, Illkirch, France. ⁵University of Geneva, Geneva, Switzerland.

⁶Tissue Biology and Disease Modelling Unit, European Molecular Biology Laboratory, Barcelona, Spain. ⁷Max Planck Institute of Molecular Cell Biology and Genetics, Dresden, Germany. ⁸Technische Universität Dresden, Biotechnologisches Zentrum, Center for Molecular Cellular Bioengineering (CMCB), Dresden, Germany. ⁹Institute of Cell Biology, University of Bern, Bern, Switzerland. ¹⁰Cluster of Excellence Physics of Life, TU Dresden, Dresden, Germany.

¹¹These authors contributed equally: Linjie Lu, Tristan Guyomar, Quentin Vagne. e-mail: riveline@unistra.fr; guillaume.salbreux@unige.ch

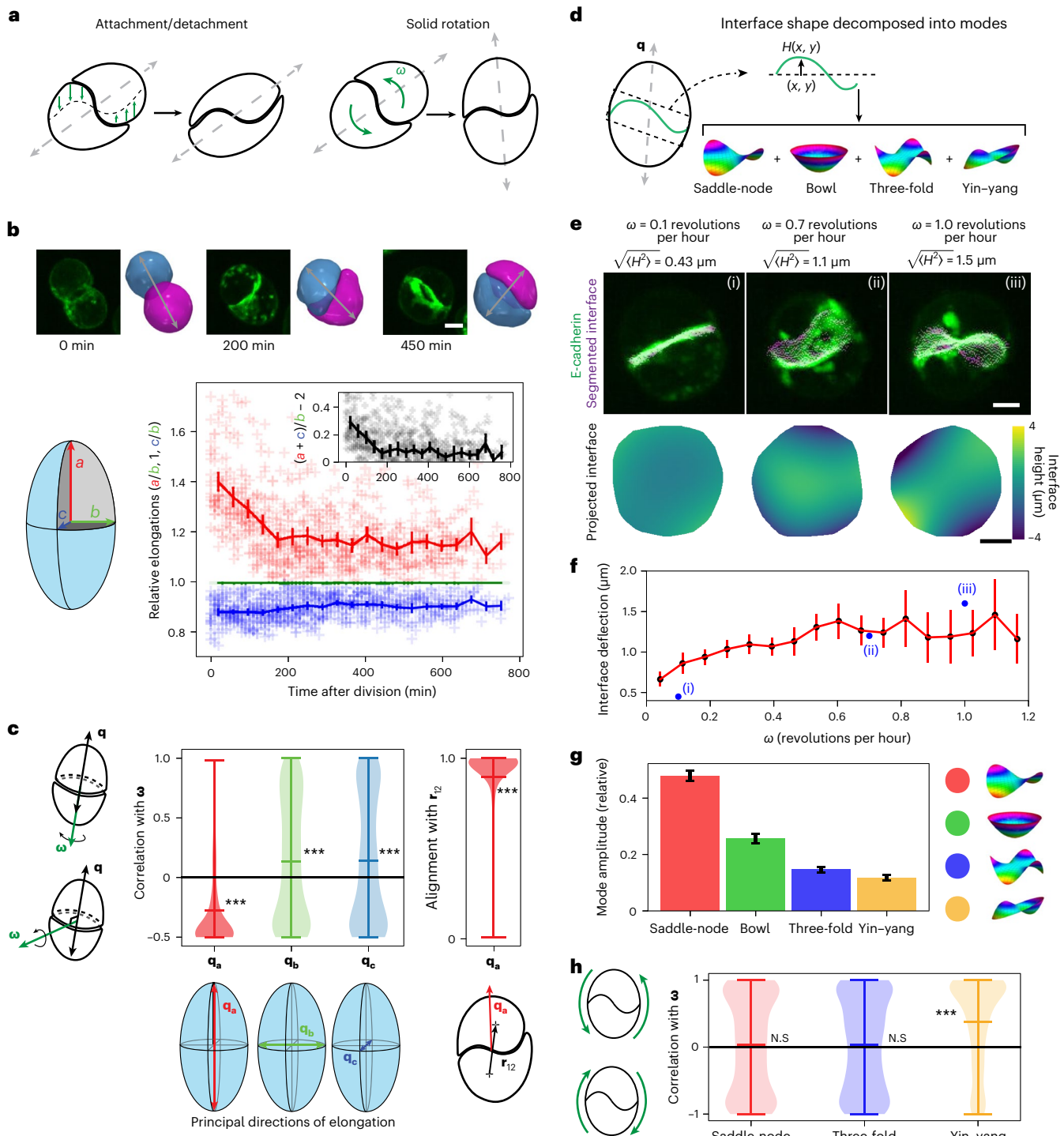
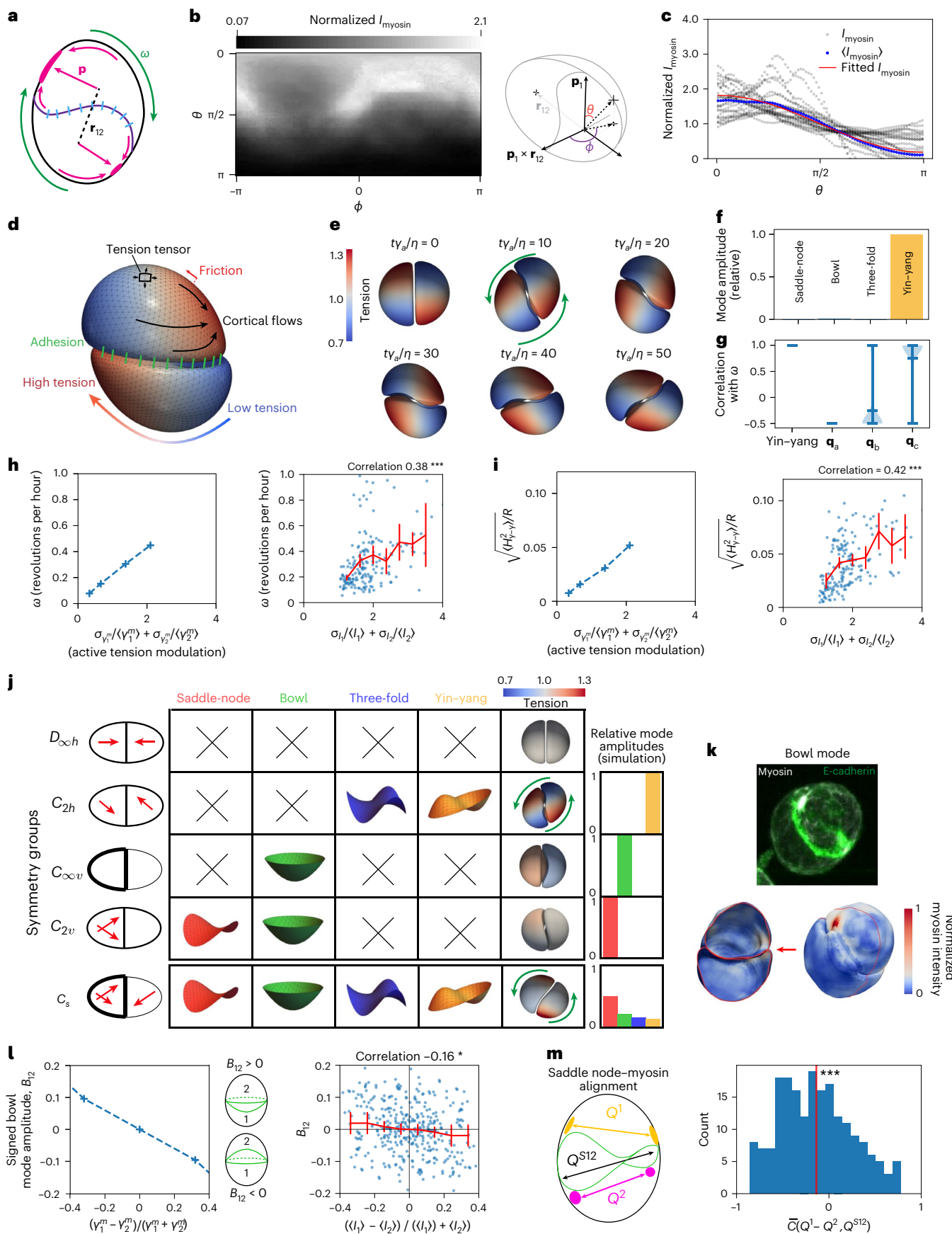


Fig. 2 | Coordinated rotation of doublet shape and interface. **a**, Schematics of possible scenarios of doublet rotation. Left: The interface is deforming (green arrows), leading to apparent rotation without motion of the doublet outer surface. Right: the doublet is rotating as a solid object and the doublet elongation axis (grey dotted line) rotates with the doublet. **b**, Top: snapshots of rotating doublets with labelled E-cadherin-mNG (green) and corresponding segmented meshes. Grey double arrows indicate the approximate elongation axis. Bottom left: a schematic for the definition of three doublet elongation axes a , b and c . Bottom right: relative doublet elongation magnitudes as a function of time after division (dots, individual data points; lines, connected binned averages). Inset: the ratio of elongation magnitudes, where positive values indicate a prolate shape. **c**, Left: the correlation of the axis of rotation with the axes of elongation $\mathbf{q} = \mathbf{q}_a$, \mathbf{q}_b , \mathbf{q}_c , as indicated in the schematics and defined in Supplementary Section 3. The direction of maximal elongation, \mathbf{q}_a , lies in the plane of rotation

of the doublet. Right: the alignment of the elongation major axis \mathbf{q}_a with the doublet axis \mathbf{r}_{12} . **d**, Schematics for decomposition of interface shape, quantified by height profile $H(x, y)$, into modes with different symmetries (colour code indicates height profile for visualization). **e**, Representative interface shape examples for different rotation magnitudes, corresponding to points indicated in **f**. Top: snapshots of E-cadherin-labelled doublets with overlaid interface segmentation, with the magnitude of the rotational velocity and average interface deflection presented above. Bottom: interface height map. **f**, The average interface deflection as a function of the magnitude of the rotational velocity. **g**, The average relative magnitude of the interface deformation modes. **h**, The correlation of the orientation of the deformation mode with the direction of rotation (indicated on the left by green arrows). Statistical tests (sign of the mean): *** $P < 10^{-4}$. Error bars show the 95% confidence interval of the mean with $n = 14$ doublets, $N = 3$ biological repeats and 780 data points in total.



Section 9.4). To test this prediction, we compared the magnitudes of the rotation and the yin–yang interface deformation mode with the variation in the cortical myosin polarity and found that they were indeed correlated (Fig. 4*h,i*). The simulated rotation magnitude was comparable to experiments for parameters giving rise to cortical flows of $\sim 0.1 \mu\text{m min}^{-1}$, comparable to the observed speed of myosin clusters (Extended Data Figs. 4d–h and 8f).

Curie principle applied to doublet interface shape

We then wondered how we could explain the emergence of modes of interface deformation other than the yin–yang shape. We reasoned that the Curie principle, stating that ‘the symmetries of the causes are to be found in the effects’^{21,22}, implies that molecular cues guiding interface deformations should satisfy symmetry rules consistent with the observed interface shape (leaving aside the possibility of spontaneous symmetry breaking). We classified a set of configurations of doublets and polarity axis according to their symmetry properties (Fig. 4j). A configuration where cell polarities are in the same plane but shifted in opposite directions away from the doublet axis belongs to the C_{2h} point group in Schoenflies notation²³. As a result, such a doublet should exhibit yin–yang and three-fold interface deformation, as observed in simulations (Fig. 4f and Extended Data Fig. 8d). In contrast, tension asymmetry between the two cells of the doublets should give rise to the bowl deformation mode. Meanwhile, a nematic configuration of active tension distribution, with different intensities in each cell, should give rise to the bowl and saddle-node deformation mode (Fig. 4j). Simulating doublets with varying profiles of active tension confirmed these predictions (Fig. 4j). We then verified if this relationship between modes of cortical myosin distribution and modes of interface deformation could be observed in experiments. Indeed, we found that the magnitude of the bowl deformation mode was correlated with the difference in the average cortical myosin intensity of the two doublet cells (Fig. 4k,l). We also noticed that the distribution of cortical myosin had a secondary, less concentrated cluster opposite to the main myosin cluster (Fig. 3n and Extended Data Fig. 7). We reasoned that this secondary cluster was giving rise to a nematic distribution of cortical myosin, quantified by a nematic tensor²⁴. Indeed, we measured a negative correlation between the nematic tensor of the saddle-node interface deformation mode and the difference of the cortical myosin nematic tensor between the two doublet cells (Fig. 4m). We then verified that simulating a doublet with an active tension profile summing a polar, nematic distribution and a difference in average tension between the two doublet cells resulted in a complex interface shape with a similar mode decomposition as in experiments (Fig. 4j, last row and Fig. 2g). We conclude that the complex shape of the doublet interface can be understood on the basis of symmetry principles from the cortical myosin distribution in the doublet.

Perturbing myosin clusters affects doublet shape and motion

We then reasoned that, if the myosin clusters are responsible for cell rotation and interface deformation, perturbing their activity and localization would affect the cell doublet shape and motion. Indeed, treatment with the myosin inhibitor blebbistatin (Fig. 5a) resulted in simultaneous rotation arrest, flattening of the interface and disappearance of clusters of phosphorylated myosin (Fig. 5a–c and Extended Data Fig. 9a,b). The effect of the blebbistatin-induced arrest of rotation was reversible. When we washed out the inhibitor, doublets retrieved rotational motion and a bent interface (Extended Data Fig. 9 and Supplementary Video 12). By incubating cells with inhibitors of Rac1 and Arp2/3 (CK666; Methods), which are key regulators of actin polymerization during single cell motility^{25,26}, we also tested whether actin polymerization was required for the rotation. Doublet rotations were arrested upon treatment but resumed after washing (Extended Data Fig. 10 and Supplementary Videos 13 and 14). This arrest was accompanied

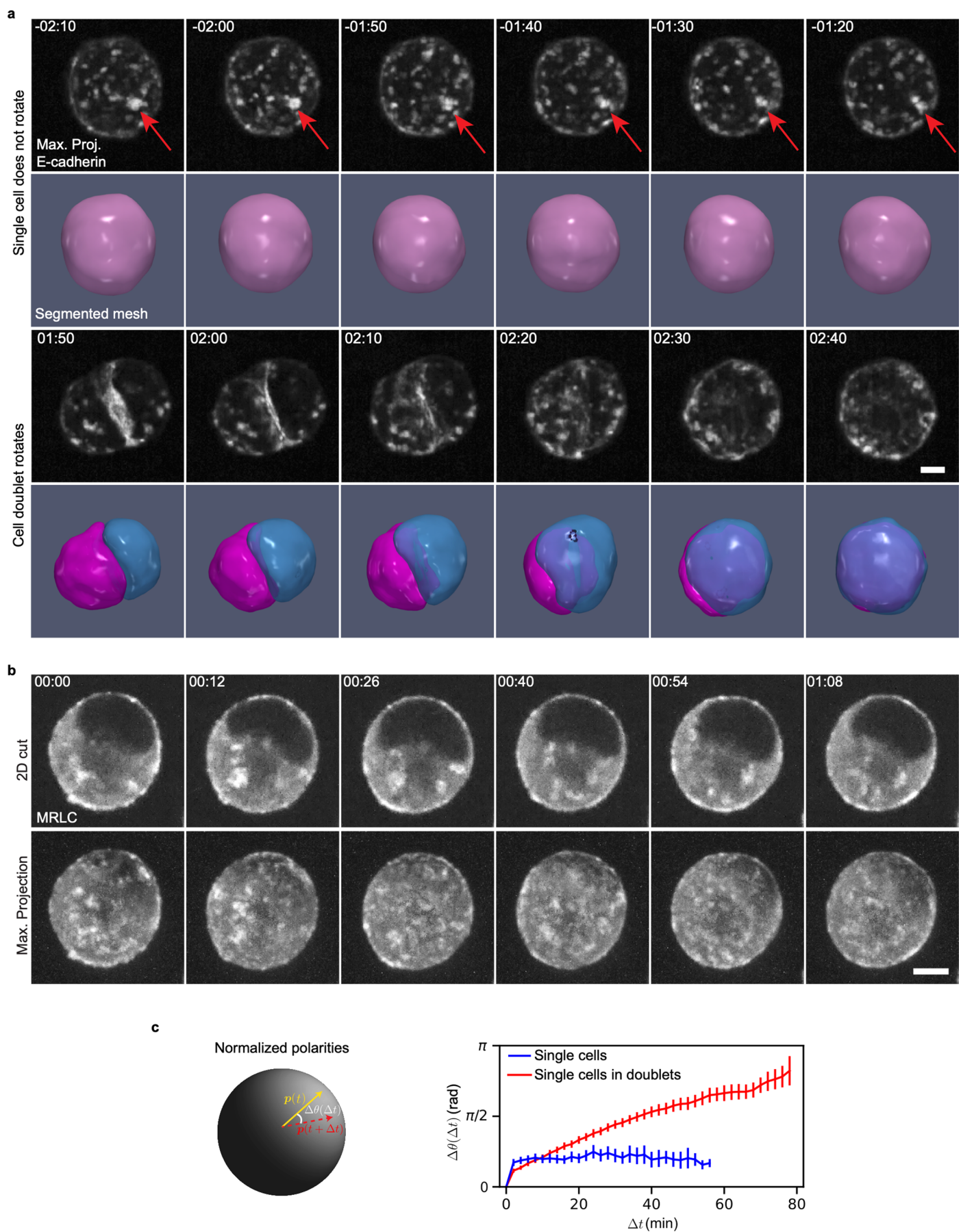
by a disassembly of myosin clusters (Extended Data Fig. 10 and Supplementary Videos 13 and 14).

We then aimed at specifically altering the two opposite myosin spots using laser ablation (Fig. 5d). This induced transient arrest of the rotation and interface flattening. Following a lag time of ~ 10 min, rotation restarted with a simultaneous increase in rotation velocity and interface deformation (Fig. 5e and Supplementary Video 15). Suppressing the gradient of active tension in the simulation also suppressed the rotation (Fig. 5d,e and Supplementary Video 16). To generate additional ectopic local myosin clusters, we then engineered a stable optogenetic cell line that we used to locally activate Rho (Fig. 5f, Supplementary Video 17 and Methods). Transient Rho activation resulted in ectopic myosin activation at the cell cortex comparable in intensity and size to spontaneous myosin clusters. This new cluster triggered the displacement of the doublet away from the region of activation while the doublet kept rotating (Fig. 5f–h). Introducing an ectopic region of increased active tension in simulations resulted in a similar drift of the doublet (Fig. 5f–h and Supplementary Video 18). Altogether, these results support the central role of myosin clusters for driving doublet rotation.

Discussion

Our analysis shows that doublet rotation arises from myosin clusters positioned away from the axis joining the two doublet cells. Therefore, the doublet cell rotation requires cell–cell interactions to trigger the shift of the cell polarity axis. Consistent with this picture, in our experimental setup, single cells do not rotate. It has been reported that, in a bilayered Matrigel, which provides an external polarization axis, single MDCK cells rotate¹¹. In this situation, the environment is providing a preferred direction. It would be interesting to track the cortical myosin distribution in cells rotating in these conditions to test whether the polarity-based mechanism we propose also applies in that context.

Which mechanisms result in myosin cluster formation? Clusters could emerge by spontaneous symmetry breaking from an initially symmetric configuration where the cell polarities are pointing towards each other (Fig. 4j). The dynamics of the increase in the rotation magnitude after cell division (Fig. 1f), which resembles an exponential increase followed by saturation, is consistent with such a scenario. The position of myosin clusters could be related to the small and transient protrusions that are sent by each cell beyond the interface at the cortex (Fig. 3f), consistent with a mechanism reported in refs. 27,28. Alternatively, they form in response to cell interface deformation and induce rotation and further cell interface deformation, with the positive feedback loop at the origin of the instability and spontaneous symmetry breaking necessary for rotation. Among the deformation modes we have analysed, the yin–yang mode has the right symmetry property to be coupled to a shift of the two cell polarities away from the doublet axis, which occurs in opposite directions in each cell of the doublet (Fig. 4j). Interestingly, we also observed that, following cell division, a myosin-dense cluster forms at the centre of the doublet interface and then appears to relocate towards the periphery of the contact (Extended Data Fig. 9c and Supplementary Video 19). We note that myosin clusters have also been reported to generate stress in cytokinesis²⁹. We also observe that focal contacts are polarized within each cell of the doublet, such that a myosin cluster in one cell is in close vicinity to a region dense in focal contacts within the opposite cell. This organization suggests either a common origin for myosin and focal contact distribution or a polarization mechanism relying on negative feedback between cortical myosin and focal contacts. Possibly, forces resulting from the inhomogeneous distribution of cortical myosin promote adhesion contacts through a reinforcement mechanism^{27,28,30,31}. Interestingly, we observed that, although E-cadherin KO doublets were still rotating, inhibition of Arp2/3 or Rac1 stopped the rotation, indicating that Arp2/3 and Rac1 activity are required for force generation by myosin in the cortex or that additional protrusive activity participates to propelling the doublet.

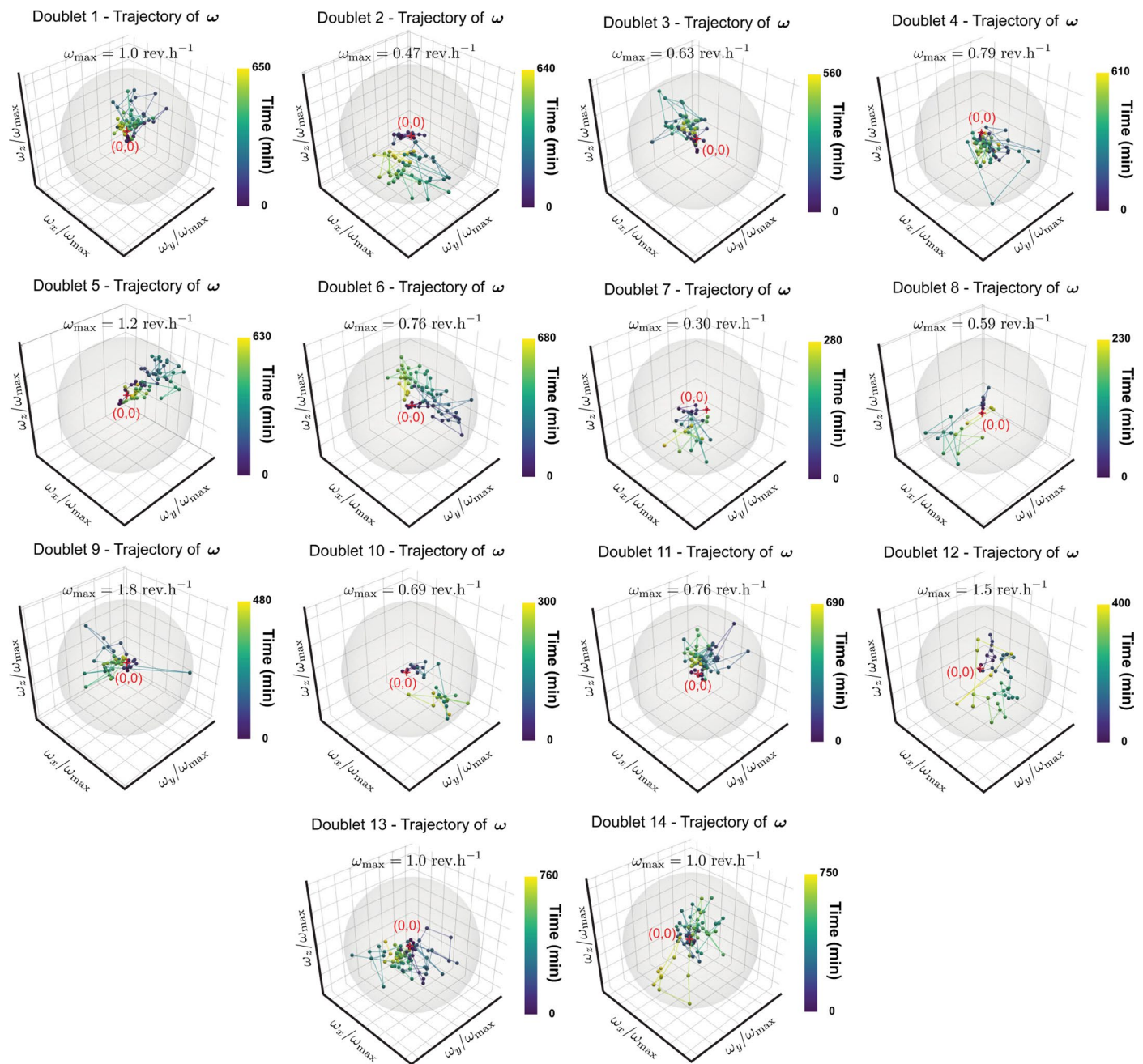


Extended Data Fig. 1 | See next page for caption.

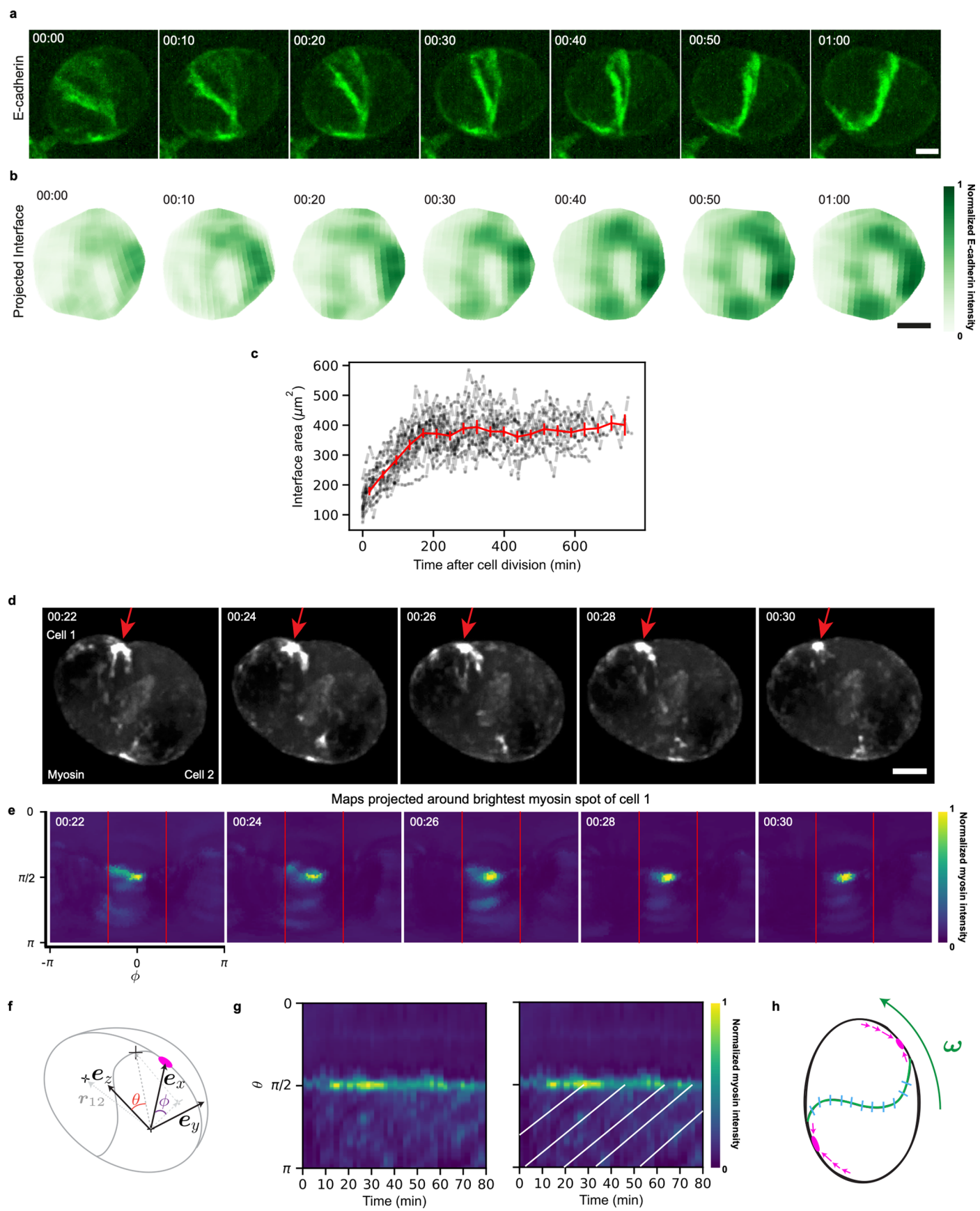
Extended Data Fig. 1 | Single cells are polarized but do not rotate.

a. Snapshot of single cell (two top rows) and cell doublet (two bottom rows). Cells labelled with E-cadherin-mNG (grey) - see beginning of Supplementary Video 2. For each case, top row: maximum projection of E-cadherin, bottom row: cell segmentation. Time relative to cell division. **b.** Snapshots of single cells labelled with MRLC-GFP (grey). Top row: cross-section, bottom row: maximum

projection. Representative example of $n > 30$ cells. **c.** Left: Myosin polarity angles $\Delta\theta$ computed between polarities at t and $t + \Delta t$. Right: Myosin polarity angles as a function of difference of time between frames Δt . Polarity of the single cell is still compared to the polarity of cells in doublets. $n = 6$ cells in doublets and $n > 10$ single cells. Scale bars: $5\mu\text{m}$. Time in hh:mm. Error bars: 95% confidence interval of the mean.



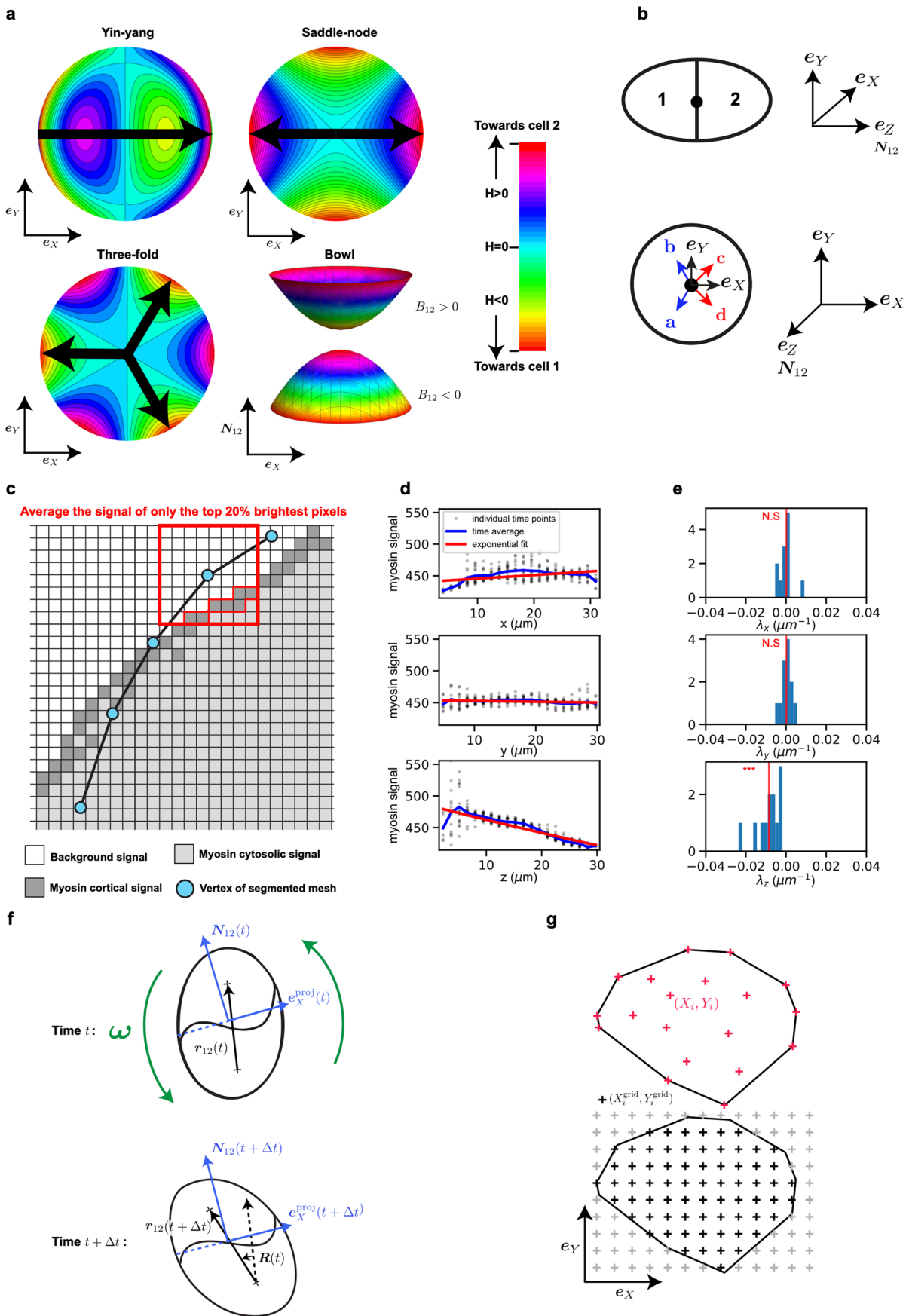
Extended Data Fig. 3 | Trajectories of rotational velocities. Similar to Fig. 1h: trajectories of the rotation vector of cell doublets after cell division for all 14 doublets, normalized with respect to their respective largest amplitudes (corresponding to Supplementary Video 2). Grey sphere has unit radius.



Extended Data Fig. 4 | See next page for caption.

Extended Data Fig. 4 | Patterns of E-cadherin at the cell-cell interface and myosin dynamics at the cortex. **a.** E-cadherin-mNG (grey) labelled rotating doublet. **b.** Patterns of E-cadherin distribution on the doublet cell-cell interface, viewed en-face, for the cell shown in a. **c.** Interface area as a function of time after cell division. $n = 14$ doublets. **d-e.** Mapping of the myosin dynamics at the cortex (procedure described in Supplementary Information section 8). Myosin clusters

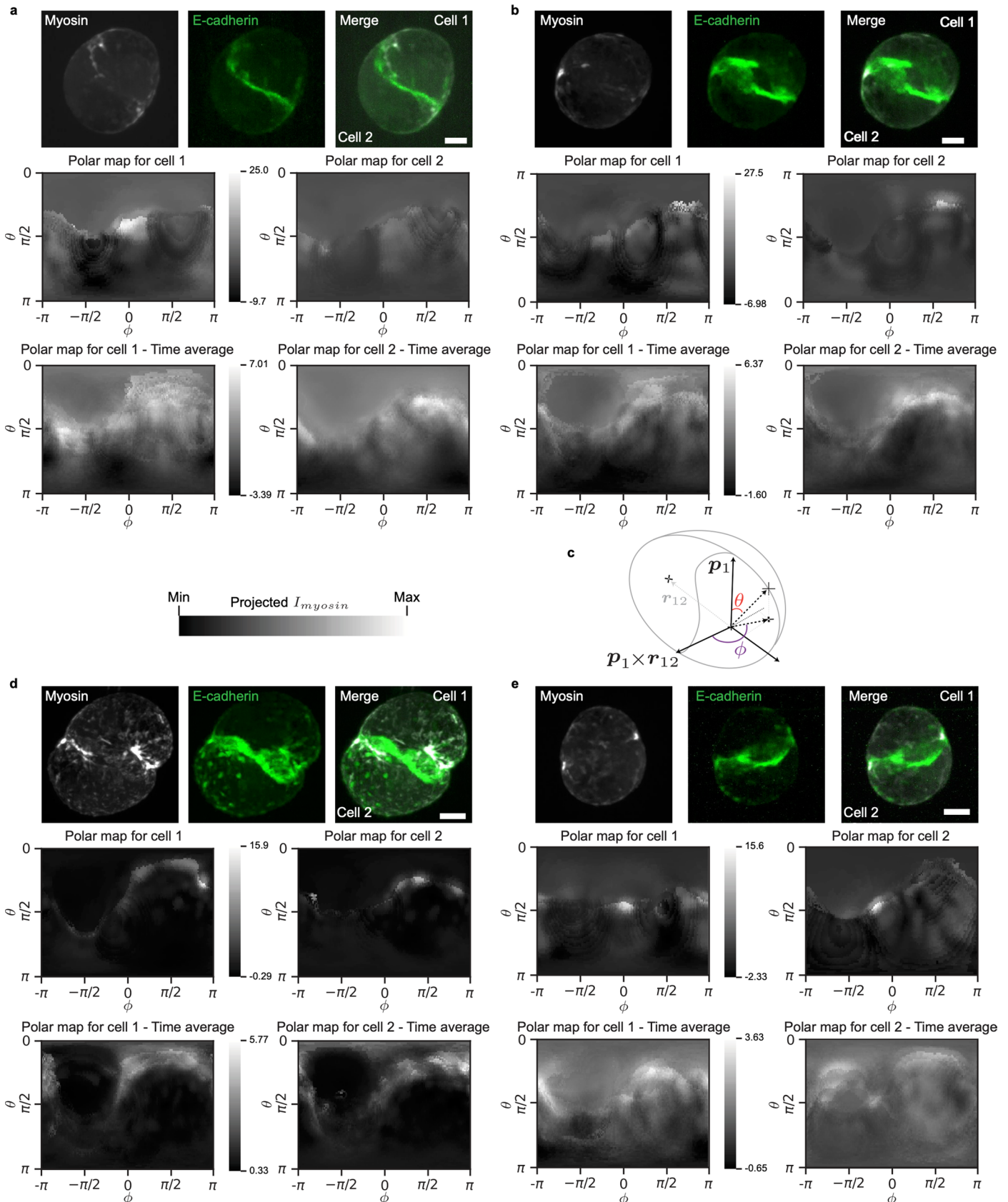
exhibit a motion towards red arrows (see Supplementary Video 8). **f.** Reference frame used to generate the maps of e. **g.** Left: Kymograph of the average between the red lines of panel e. Right: Similar kymograph with white lines indicating motion of myosin clusters with a velocity of about $0.3 \mu\text{m}/\text{min}$. **h.** Schematics for myosin clusters motion (purple) and cadherin (blue) distribution. Scale bars: $5 \mu\text{m}$. Time in hh:mm.



Extended Data Fig. 5 | See next page for caption.

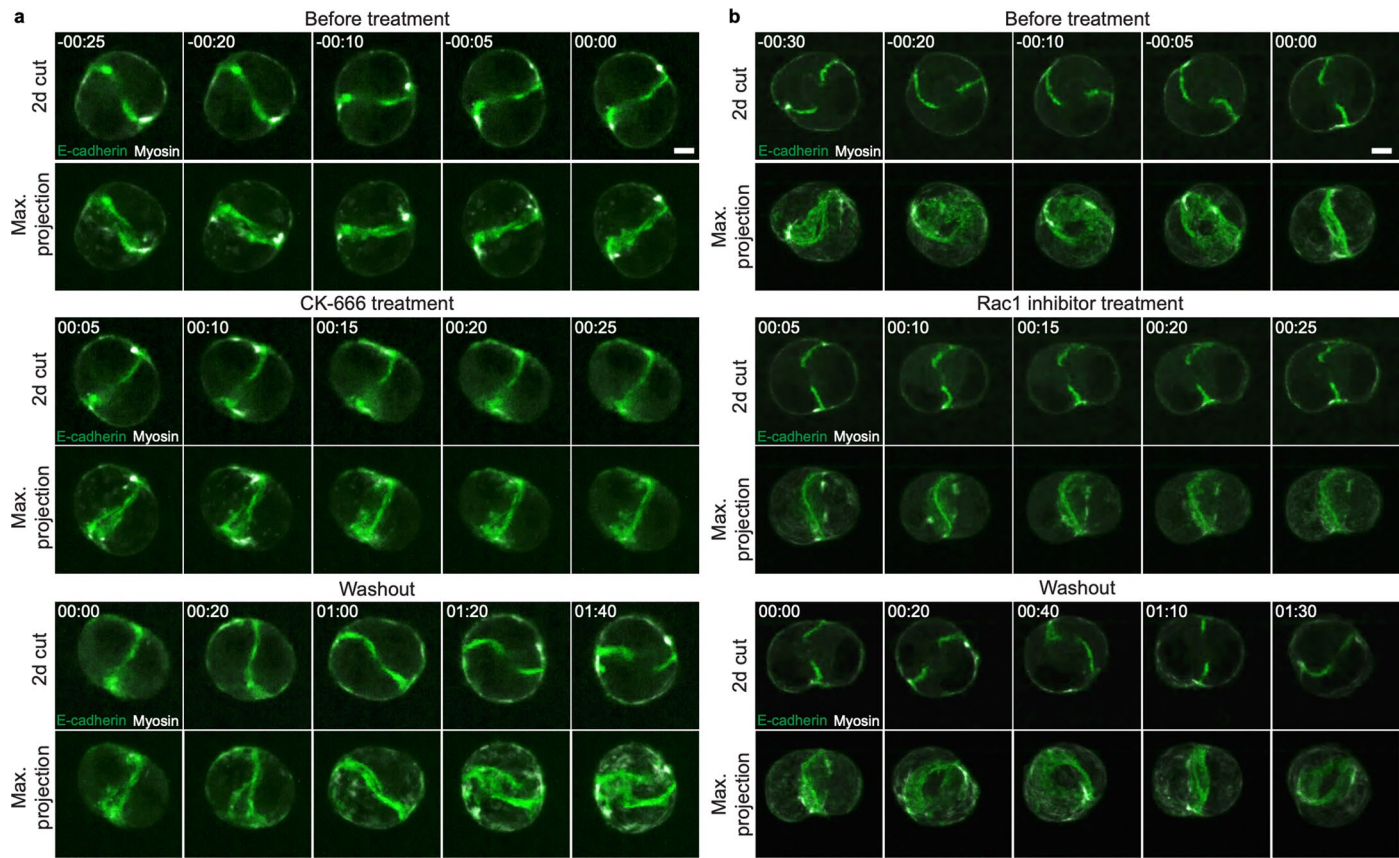
Extended Data Fig. 5 | Analysis of interface shape. **a.** Height profile of interface deformation modes. The yin-yang orientation is characterized by a vector, the saddle-node by a nematic, and the three-fold by a three-fold orientational order. **b.** Schematic for the orientation of the vectors ($\mathbf{e}_x, \mathbf{e}_y, \mathbf{e}_z = \mathbf{N}_{12}$) associated to the interface of the cell doublet. The vectors $\mathbf{a}, \mathbf{b}, \mathbf{c}, \mathbf{d}$ are introduced to define transformations in Supplementary Table 1. **c.** Schematics of method used to obtain cortical intensities from cell segmentation (see Supplementary Information section 5.1) **d.** Average profile of myosin fluorescence intensity in the x, y, z directions, for a representative doublet. **e.** Histogram of fitting

parameters characterizing the average myosin profiles, as in d, for all doublets. Only λ_z is significantly different from 0. **f,g.** Procedure to create interfacial E-cadherin maps shown in Extended Fig. 4b. **f.** A reference vector $\mathbf{e}_X^{\text{proj}}$ is rotated with the doublet (using the rotation $\mathbf{R}(t)$ of the \mathbf{r}_{12} vector) to define a consistent viewpoint and is projected at each time t in the plane of the interface defined by \mathbf{N}_{12} . **g.** (Top) 2D coordinates (X_i, Y_i) of the interface vertices i, surrounded by their convex hull. (Bottom) A regular grid of new coordinates ($X_i^{\text{grid}}, Y_i^{\text{grid}}$) is created inside the convex hull (black points). Statistical test (sign of the mean): panel e: $\lambda_x: p = 0.41 \pm 0.01, \lambda_y: p = 0.404 \pm 0.009, \lambda_z: ***, p < 10^{-4}$.

**Extended Data Fig. 7 | Example of polar maps of cortical myosin intensity.**

a,b,d,e. Maps of experimental myosin intensity after calibration in spherical coordinates, in a reference frame defined by the polarity axis p , the axis of the doublet r_{12} and their cross-product. For each example, top row: snapshot of doublet, maximum projections of myosin (MRLC-GFP), E-cadherin (Ecadherin-mNG) and

merge, middle row: individual cell maps corresponding to the above snapshot, bottom row: time average cell maps corresponding to the time series from which the snapshot in the top row was taken from. **c.** Scheme of the reference frame. Scale bar: 5 μ m. Procedure described in Supplementary Information section 5.6.



Extended Data Fig. 10 | Interfering with actin dynamics affects doublet rotation. **a.** Snapshots of a rotating doublet in the presence of the Arp2/3 inhibitor CK-666 before and after incubation followed by washout (see Supplementary Video 13). E-cadherin (green), myosin (grey). Representative example of n > 10 doublets. **b.** Snapshots of a rotating doublet in the presence of Rac1 inhibitor before and after incubation followed by washout (see Supplementary Video 14). E-cadherin (green). Myosin (grey). Representative example of n > 10 doublets. Scale bars: 5 μ m. Time in hh:mm.

Daniel Rivelin, Guillaume Salbreux

riveline@unistra.fr,

guillaume.salbreux@unige.ch

Corresponding author(s):

Last updated by author(s): 29/01/2024

Reporting Summary

Nature Portfolio wishes to improve the reproducibility of the work that we publish. This form provides structure for consistency and transparency in reporting. For further information on Nature Portfolio policies, see our [Editorial Policies](#) and the [Editorial Policy Checklist](#).

Statistics

For all statistical analyses, confirm that the following items are present in the figure legend, table legend, main text, or Methods section.

n/a Confirmed

- The exact sample size (n) for each experimental group/condition, given as a discrete number and unit of measurement
- A statement on whether measurements were taken from distinct samples or whether the same sample was measured repeatedly
- The statistical test(s) used AND whether they are one- or two-sided
Only common tests should be described solely by name; describe more complex techniques in the Methods section.
- A description of all covariates tested
- A description of any assumptions or corrections, such as tests of normality and adjustment for multiple comparisons
- A full description of the statistical parameters including central tendency (e.g. means) or other basic estimates (e.g. regression coefficient) AND variation (e.g. standard deviation) or associated estimates of uncertainty (e.g. confidence intervals)
- For null hypothesis testing, the test statistic (e.g. F , t , r) with confidence intervals, effect sizes, degrees of freedom and P value noted
Give P values as exact values whenever suitable.
- For Bayesian analysis, information on the choice of priors and Markov chain Monte Carlo settings
- For hierarchical and complex designs, identification of the appropriate level for tests and full reporting of outcomes
- Estimates of effect sizes (e.g. Cohen's d , Pearson's r), indicating how they were calculated

Our web collection on [statistics for biologists](#) contains articles on many of the points above.

Software and code

Policy information about [availability of computer code](#)

Data collection

Metamorph was used to acquire the images on a Leica Spinning Disk microscope as described in the Methods section.
Simulation results were generated using a custom C++ code adapted from a previously published code available at <https://github.com/torressancheza/ias>.

Data analysis

FIJI was used to contrast and overlay images.
Cell segmentation was performed with previously published FIJI plugin LimeSeg 0.4.2 (<https://imagej.net/plugins/limeseg>).
All quantifications and data analysis were then performed using custom Python codes as described in the Methods section and Supplementary Information.
Visualisation and rendering of 3D meshes were performed using Paraview Software 5.10.1.
All plots were generated with Python (version 3.9.10).

For manuscripts utilizing custom algorithms or software that are central to the research but not yet described in published literature, software must be made available to editors and reviewers. We strongly encourage code deposition in a community repository (e.g. GitHub). See the Nature Portfolio [guidelines for submitting code & software](#) for further information.

Data

Policy information about [availability of data](#)

All manuscripts must include a [data availability statement](#). This statement should provide the following information, where applicable:

- Accession codes, unique identifiers, or web links for publicly available datasets
- A description of any restrictions on data availability
- For clinical datasets or third party data, please ensure that the statement adheres to our [policy](#)

All data are available upon request to the corresponding authors.

Human research participants

Policy information about [studies involving human research participants and Sex and Gender in Research](#).

Reporting on sex and gender

n/a

Population characteristics

n/a

Recruitment

n/a

Ethics oversight

n/a

Note that full information on the approval of the study protocol must also be provided in the manuscript.

Field-specific reporting

Please select the one below that is the best fit for your research. If you are not sure, read the appropriate sections before making your selection.

Life sciences

Behavioural & social sciences

Ecological, evolutionary & environmental sciences

For a reference copy of the document with all sections, see nature.com/documents/nr-reporting-summary-flat.pdf

Life sciences study design

All studies must disclose on these points even when the disclosure is negative.

Sample size

All quantifications were performed for at least n=12 cell doublets, except for Fig. 5b,c (4 doublets), Fig.5e (9 doublets), Fig. 5g,h (9 doublets) and Ext. Fig. 1c (red curve, 6 doublets).

Data exclusions

No points were excluded from the data analysis.

Replication

All experiments were systematically performed at least 3 times and gave similar results.

Randomization

Cell doublets were chosen to be imaged randomly among a large population. The subset of doublets used for segmentation were chosen randomly among those with a rotation axis approximatively aligned with the microscope Z-axis (with random clockwise or counterwise rotation). This allowed better segmentation of cells.

Blinding

n/a

Reporting for specific materials, systems and methods

We require information from authors about some types of materials, experimental systems and methods used in many studies. Here, indicate whether each material, system or method listed is relevant to your study. If you are not sure if a list item applies to your research, read the appropriate section before selecting a response.

Materials & experimental systems

n/a	Involved in the study
<input type="checkbox"/>	<input checked="" type="checkbox"/> Antibodies
<input type="checkbox"/>	<input checked="" type="checkbox"/> Eukaryotic cell lines
<input checked="" type="checkbox"/>	<input type="checkbox"/> Palaeontology and archaeology
<input checked="" type="checkbox"/>	<input type="checkbox"/> Animals and other organisms
<input checked="" type="checkbox"/>	<input type="checkbox"/> Clinical data
<input checked="" type="checkbox"/>	<input type="checkbox"/> Dual use research of concern

Methods

n/a	Involved in the study
<input checked="" type="checkbox"/>	<input type="checkbox"/> ChIP-seq
<input checked="" type="checkbox"/>	<input type="checkbox"/> Flow cytometry
<input checked="" type="checkbox"/>	<input type="checkbox"/> MRI-based neuroimaging

Antibodies

Antibodies used

- 1. Rat monoclonal Anti-E-cadherin, Abcam, Cat# Ab11512.
- 2. Rabbit Polyclonal Anti-Phospho-Myosin Light Chain2 (Cell signaling technology, #3674).
- 3. Rabbit monoclonal Anti-Paxillin (Abcam, Ab32084).
- 4. Alexa FluorTM 357 Phalloidin 488 (Thermo Fisher, A12379).

Validation

Validated by the Companies.

Eukaryotic cell lines

Policy information about [cell lines and Sex and Gender in Research](#)

Cell line source(s)

1. MDCK II VASP-GFP (see ref. 34).
2. MDCK II MRLC-KO1/E-cadherin-mNG and MDCK II MRLC-GFP (Riveline Lab.).
3. MDCK II E-cadherin-GFP and MDCK II E-cadherin-DsRed (from Nelson, see ref. 37).
4. MDCK II E-cadherin-GFP/Podocalyxin-mScarlett/Halo-CAAX (engineered in Honigmann Lab)
5. MDCK II iLID-LARG::mVenus - 2xrgBD-dTomato - MRLC-iRFP703 (optogenetic cell line, Riveline Lab.).
6. MDCK II Actin-GFP (Nelson Lab)
7. MDCK II Lifeact-iRFP (Riveline Lab)
8. MDCK II E-cadherin-KO (from Ladoux lab, ref. 16)

Authentication

From the sources.

Mycoplasma contamination

All cell lines were checked for the absence of mycoplasma contamination.

Commonly misidentified lines (See [ICLAC](#) register)

No commonly misidentified cell lines were used in the study.